

Epitaxial $\text{Zn}_x\text{Fe}_{3-x}\text{O}_4$ Thin Films: A Spintronic Material with Tunable Electrical and Magnetic Properties

Deepak Venkateshvaran,^{1,2} Matthias Althammer,¹ Andrea Nielsen,¹ Stephan Geprags,¹ M.S. Ramachandra Rao,^{2,3} Sebastian T. B. Goennenwein,¹ Matthias Opel,^{1,*} and Rudolf Gross^{1,4,†}

¹Walther-Meißner-Institut, Bayerische Akademie der Wissenschaften, 85748 Garching, Germany

²Materials Science Research Centre, Indian Institute of Technology Madras, Chennai 600036, India

³Physics Department, Indian Institute of Technology Madras, Chennai 600036, India

⁴Physik-Department, Technische Universitat Munchen, 85748 Garching, Germany

(Dated: October 30, 2018)

The ferrimagnetic spinel oxide $\text{Zn}_x\text{Fe}_{3-x}\text{O}_4$ combines high Curie temperature and spin polarization with tunable electrical and magnetic properties, making it a promising functional material for spintronic devices. We have grown epitaxial $\text{Zn}_x\text{Fe}_{3-x}\text{O}_4$ thin films ($0 \leq x \leq 0.9$) on $\text{MgO}(001)$ substrates with excellent structural properties both in pure Ar atmosphere and an Ar/O₂ mixture by laser molecular beam epitaxy and systematically studied their structural, magnetotransport and magnetic properties. We find that the electrical conductivity and the saturation magnetization can be tuned over a wide range ($10^2 \dots 10^4 \Omega^{-1}\text{m}^{-1}$ and $1.0 \dots 3.2 \mu\text{B}/\text{f.u.}$ at room temperature) by Zn substitution and/or finite oxygen partial pressure during growth. Our extensive characterization of the films provides a clear picture of the underlying physics of the spinel ferrimagnet $\text{Zn}_x\text{Fe}_{3-x}\text{O}_4$ with antiparallel Fe moments on the *A* and *B* sublattice: (i) Zn substitution removes both Fe_A^{3+} moments from the *A* sublattice and itinerant charge carriers from the *B* sublattice, (ii) growth in finite oxygen partial pressure generates Fe vacancies on the *B* sublattice also removing itinerant charge carriers, and (iii) application of both Zn substitution and excess oxygen results in a compensation effect as Zn substitution partially removes the Fe vacancies. Both electrical conduction and magnetism is determined by the density and hopping amplitude of the itinerant charge carriers on the *B* sublattice, providing electrical conduction and ferromagnetic double exchange between the mixed-valent $\text{Fe}_B^{2+}/\text{Fe}_B^{3+}$ ions on the *B* sublattice. A decrease (increase) of charge carrier density results in a weakening (strengthening) of double exchange and thereby a decrease (increase) of conductivity and the saturation magnetization. This scenario is confirmed by the observation that the saturation magnetization scales with the longitudinal conductivity. The combination of tailored $\text{Zn}_x\text{Fe}_{3-x}\text{O}_4$ films with semiconductor materials such as ZnO in multi-functional heterostructures seems to be particularly appealing.

PACS numbers: 75.70.-i 81.15.Fg, 85.75.-d 75.50.Dd

1. INTRODUCTION

Spintronic materials and devices are in the focus of current research activities^{1,2}. Regarding functional spintronic materials, transition metal oxides are promising candidates, since they show a rich variety of electrical and magnetic properties specifically interesting for applications in spintronics. Evidently, useful spintronic devices such as magnetoresistive elements based on the tunneling magnetoresistance³ or spin transistors⁴ require ferromagnetic materials with high Curie temperature T_C well above room temperature and large spin polarization P of the charge carriers at the Fermi level E_F . Moreover, advanced applications often require materials with magnetic properties which can be deliberately tuned by external control parameters such as an applied electric field⁵, elastic stress^{6,7}, or light⁸. In this respect, Fe_3O_4 (magnetite) is a highly promising candidate. First, it has both a high Curie temperature of $T_C \simeq 860\text{K}$ and according to band structure calculations is expected a half-metal⁹ corroborated by spin-resolved photoelectron spectroscopy^{10,11}. Second, recent experiments indicated that both the electronic and magnetic properties of Fe_3O_4 thin films can be nicely tailored in solid solu-

tion systems of $\text{Fe}_{3-x}\text{M}_x\text{O}_4$ ($M = \text{Zn}, \text{Mn}$)^{12,13}. Third, it has been demonstrated that the magnetic anisotropy of Fe_3O_4 can be tuned by elastic stress imposed by a piezoelectric actuator¹⁴. Taken all together, due to their interesting, versatile, and tunable properties magnetite thin films and heterostructures became the focus of recent research activities.

Before discussing the various possibilities for tuning and tailoring the electronic and magnetic properties of magnetite we briefly review its basic structural and magnetic properties. Magnetite is known to have an inverse spinel structure as shown in Fig. 1(a). The *A* sites (8 per unit cell), which are surrounded by oxygen tetrahedra, are occupied by trivalent Fe_A^{3+} ions ($3d^5, S = 5/2$), whereas on the octahedrally coordinated *B* sites (16 per unit cell) there is an alternating arrangement of Fe_B^{2+} ($3d^6, S = 2$) and Fe_B^{3+} ($3d^5, S = 5/2$) ions. Therefore, the sum formula of magnetite can be expressed as $[\text{Fe}^{3+}]_A[\text{Fe}^{3+}\text{Fe}^{2+}]_B\text{O}_4$. The density of itinerant charge carriers is determined by the density of the t_{2g} spin-down electron on the *B* site, i.e. by the density of Fe_B^{2+} . The magnetic exchange in magnetite is governed by a combination of antiferromagnetic superexchange (SE) and ferromagnetic double exchange (DE) interactions. There

are three antiferromagnetic SE interactions J_{AA} (A-O-A), J_{BB} (B-O-B), and J_{AB} (A-O-B) between the Fe^{3+} ions on the A and B sites mediated by the oxygen (O) ions. In addition, there is a ferromagnetic DE interaction mediated by the itinerant spin-down t_{2g} electrons hopping between the mixed-valent Fe ions on the B sites (cf. Fig. 1). Owing to Hund's rule coupling, the spins of these itinerant electrons are antiferromagnetically coupled to the localized spins formed by the $3d$ spin-up electrons. As pointed out by Néel¹⁵, in the simplest model ferrimagnetism in Fe_3O_4 with high T_C is obtained without any DE interaction for large $J_{AB} \gg J_{BB}, J_{AA}$ forcing an antiparallel alignment of the moments on the A and B sites (see Fig. 1(b)). Since the antiparallel Fe_A^{3+} and Fe_B^{3+} moments compensate each other, a saturation magnetization of $4\mu_B$ /formula unit (f.u.) is expected from the remaining Fe_B^{2+} ($S = 2$) moments. Later on, the simple Néel model has been extended by Yafet and Kittel¹⁶. They proposed a more elaborate model in which the B sublattice is subdivided into two Fe_B^{2+} and Fe_B^{3+} sublattices. It was shown that on weakening J_{AB} and strengthening J_{BB} , the B site magnetic moments are no longer rigidly parallel to the A site moments. The stronger B-O-B SE interaction results in spin canting expressed by a finite Yafet-Kittel angle and thus a reduction of the saturation magnetization. More recent models show that a detailed modelling of the magnetic properties of magnetite is only possible by taking into account the ferromagnetic DE interaction of the B sublattice competing with the antiferromagnetic SE^{17,18,19}.

There are several possibilities to tailor the magnetic properties of magnetite. First, Fe_A^{3+} on the A site can be replaced by an isovalent nonmagnetic ion. In this way antiferromagnetically coupled moments on the A sites are removed without affecting the magnetic exchange on the B sublattices. Hence, an increase of the saturation magnetization is expected at low substitution level. However, on increasing the A site substitution the dilution of the A site moments reduces J_{AB} , whereas J_{BB} stays about constant. Then the moments on the A and B site do no longer need to be rigidly antiparallel, resulting in a finite Yafet-Kittel angle (see Fig. 1(c) and (d)). This angle increases with increasing substitution, resulting in a reduction of the saturation magnetization. Due to the isovalent substitution the charge carrier density should stay unaffected. However, the hopping between the mixed-valent ($\text{Fe}_B^{2+}/\text{Fe}_B^{3+}$) ions on the B sublattice is reduced due to the spin canting, resulting in a lower electrical conductivity and reduced DE interaction. To our knowledge a nonmagnetic isovalent A site substitution in Fe_3O_4 has not been reported so far. Most likely this can be attributed to the fact that suitable trivalent ions usually prefer the octahedral coordination on the B site and thus cannot be substituted solely on the tetrahedral A site. Second, as done in our work, Fe_A^{3+} on the A site can be replaced by a nonmagnetic divalent ion such as Zn^{2+} ($3d^{10}, S = 0$)²⁰. It is known that Zn^{2+} preferably occupies the tetrahedrally coordinated A site in the inverse

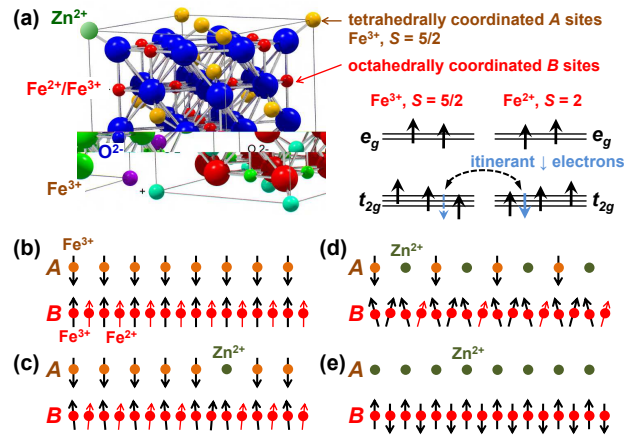


FIG. 1: (color online) (a) Inverse spinel structure of magnetite with Fe_A^{3+} on the tetrahedrally coordinated A site and mixed-valent Fe_B^{2+} ($3d^6, S=2$)/ Fe_B^{3+} ($3d^5, S = 5/2$) ions on the octahedrally coordinated B site. Zn substitution replaces Fe_A^{3+} on the A site by nonmagnetic Zn^{2+} ($3d^{10}, S = 0$) ions. Also shown is the occupation of the Fe_B^{2+} and Fe_B^{3+} $3d$ states with t_{2g} and e_g symmetry separated by the crystal field splitting due to the octahedral oxygen surrounding. The t_{2g} spin-down electron can hop between Fe_B^{2+} and Fe_B^{3+} ions with its spin coupled anti-parallel to the local moment formed by the spin-up electrons owing to Hund's rule coupling. (b) - (e) shows the A and B sublattice configuration for $\text{Zn}_x\text{Fe}_{3-x}\text{O}_4$ for (b) $x = 0$, (c) $x = 1/8$, (d) $x = 0.5$, and (e) $x = 1$.

spinel structure²¹. Again some of the antiferromagnetically coupled moments on the A sites are removed, leading to an initial increase of the saturation magnetization at low Zn substitution^{12,22}. However, in the same way as discussed before, a finite Yafet-Kittel angle and, in turn, a reduction of the saturation magnetization is expected going to larger substitution levels²². Moreover, substitution of Fe_A^{3+} by Zn^{2+} on the A site also reduces the amount of Fe_B^{2+} on the B site due to charge neutrality. That is, the amount of itinerant charge carriers mediating the DE on the B sublattice is reduced as shown by photoemission spectroscopy¹³. Thus, with increasing Zn substitution the electrical conductivity is reduced both by a reduction of the density of itinerant charge carriers and their hopping amplitude due to spin canting. Third, Fe vacancies can be introduced by preparing magnetite samples in excess oxygen^{20,23,24,25,26}. Since Fe vacancies are formally equivalent to the presence of excess of O^{2-} ions, charge neutrality again requires a reduced (increased) amount of Fe_B^{2+} (Fe_B^{3+}) ions on the B site. This strengthens antiferromagnetic SE and weakens ferromagnetic DE on the B sublattice. In turn, this results in a finite Yafet-Kittel angle and a reduced saturation magnetization. Furthermore, a reduced electrical conductivity is expected both by a reduced carrier density and hopping amplitude.

Our brief discussion shows that Fe based magnetic

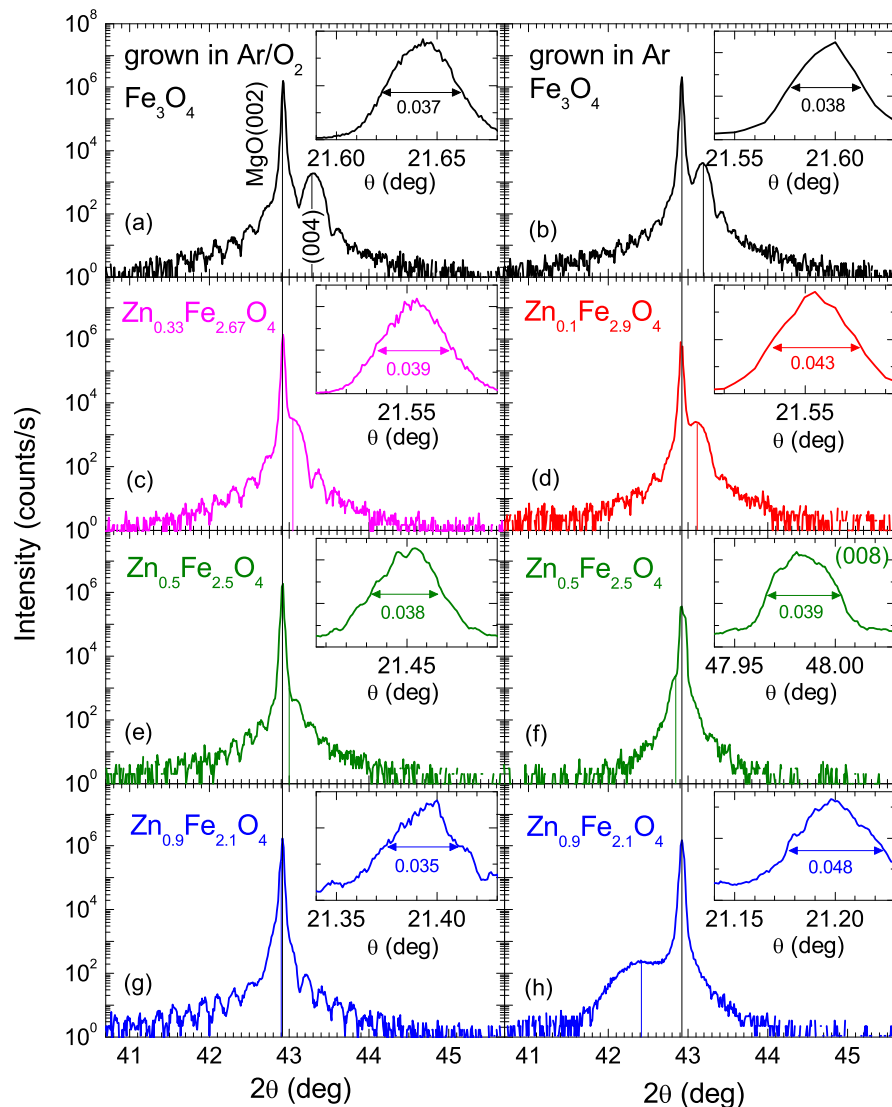


FIG. 2: (color online) X-ray diffraction diagrams (ω - 2θ scans) of the out-of-plane reflections from $\text{Zn}_x\text{Fe}_{3-x}\text{O}_4$ thin films deposited in different growth atmospheres of Ar/ O_2 (99:1) (left panels) and pure Ar (right panels). With increasing x the $\text{Zn}_x\text{Fe}_{3-x}\text{O}_4$ (004) reflection shifts across the (002) reflection of the MgO substrates marked by the vertical line. The insets show the corresponding rocking curves of the $\text{Zn}_x\text{Fe}_{3-x}\text{O}_4$ (004) reflection, except for (f) where the $\text{Zn}_x\text{Fe}_{3-x}\text{O}_4$ (008) reflection is displayed.

oxides with spinel structure are interesting materials. They do not only have high Curie temperature and high spin polarization but also offer various opportunities to tailor their electrical (charge carrier density, electrical conductivity) and magnetic properties (saturation magnetization, Curie temperature). Such tunable ferromagnetic materials are desired for spintronic devices operating at room temperature. For example, tuning the electrical conductivity of ferromagnetic materials with high spin polarization is promising for spin injection devices as one can reduce and deliberately choose the conductivity mismatch between semiconductors and ferromagnetic spin injectors. To this end, recently the growth of epitaxial $\text{Fe}_3\text{O}_4/\text{ZnO}$ heterostruc-

tures has been demonstrated²⁷. Here, we report on the growth as well as the structural, magnetic and magnetotransport properties of epitaxial thin film samples of $\text{Zn}_x\text{Fe}_{3-x}\text{O}_4$ with $x = 0, 0.1, 0.33, 0.5, 0.9$ deposited in different oxygen partial pressure. We show that their saturation magnetization and electrical conductivity can be tuned over a wide range both by Zn substitution and varying oxygen partial pressure during growth. Furthermore, our systematic study provides clear evidence that their electrical conductivity is closely related to the overall magnetization. We also carefully consider the presence of anti-phase boundaries (APBs) in the thin film samples which could affect both their electrical conductivity and their saturation magnetization^{28,29}. However,

we have clear evidence that APBs do not play a dominant role in this study. In particular, they cannot explain the change of the magnetic and magnetotransport properties on varying the Zn content and the deposition atmosphere. In contrast, these properties can be consistently explained solely by disorder and spin canting on the B sublattice, tending to localize the itinerant charge carriers on the B sublattice.

2. THIN FILM GROWTH

Epitaxial thin films of $\text{Zn}_x\text{Fe}_{3-x}\text{O}_4$ with $x \leq 0.9$ and thicknesses between 40 nm and 60 nm were deposited from stoichiometric targets on single crystalline, (001) oriented MgO substrates by laser molecular beam epitaxy (laser-MBE)³⁰. The exact film thickness was determined by x-ray reflectometry. Both bulk Fe_3O_4 having an inverse spinel structure ($Fd\bar{3}m$) and MgO ($Fm\bar{3}m$) are cubic with lattice constants of $a_{\text{Fe}_3\text{O}_4} = 8.394 \text{ \AA}$ ³¹ and $a_{\text{MgO}} = 4.212 \text{ \AA}$, respectively, resulting in a small lattice mismatch of $(a_{\text{Fe}_3\text{O}_4} - 2a_{\text{MgO}})/2a_{\text{MgO}} = -0.4\%$. The energy density of the KrF excimer laser ($\lambda = 248 \text{ nm}$) at the target was 3.1 J/cm^2 and the laser repetition rate 2 Hz. At the same total pressure of $3.7 \times 10^{-3} \text{ mbar}$, two sets of samples were deposited in two different growth atmospheres. In pure Ar, thin films with $x = 0, 0.1, 0.5$, and 0.9 were grown at a substrate temperature of 320°C . In an Ar/O₂ (99:1) mixture, thin films with $x = 0.5$ were deposited at 320°C and with $x = 0, 0.33$, and 0.9 at 400°C . The growth process was monitored *in-situ* by reflection high energy electron diffraction (RHEED)³². We observed four RHEED intensity oscillations per unit cell, indicating a block-by-block growth mode with four charge neutral blocks. This is already known for Fe_3O_4 ^{33,34} and also holds when substituting Zn up to $\text{Zn}_{0.9}\text{Fe}_{2.1}\text{O}_4$. A more detailed description of the thin film deposition for Fe_3O_4 on MgO is given elsewhere^{33,35}.

3. STRUCTURAL PROPERTIES

The structural properties of the $\text{Zn}_x\text{Fe}_{3-x}\text{O}_4$ films were analyzed by high resolution x-ray diffractometry using a Bruker AXS D8 Discover four-circle diffractometer. Our detailed analysis reveals a very high epitaxial quality of all thin film samples. In $[00\ell]$ direction, ω - 2θ scans display no impurity phases - in particular from other iron or zinc oxides. We note that we may not be able to distinguish between Fe_3O_4 and $\gamma\text{-Fe}_2\text{O}_3$ (maghemite) as they both share the same inverse spinel lattice³⁶. It is known that excess oxygen results in the formation of Fe vacancies and in the extreme case to formation of $\text{Fe}_3\text{O}_4/\gamma\text{-Fe}_2\text{O}_3$ solid solutions^{24,25}. The $\text{Fe}_3\text{O}_4/\gamma\text{-Fe}_2\text{O}_3$ thermodynamic equilibrium line was determined to $\log(p_{\text{O}_2}/p_0) = -\frac{24,634\text{K}}{T}$ with $p_0 = 9.1 \times 10^{13} \text{ bar}$ ²⁴. Unfortunately, both calculations and experimental studies of phase and point defect equilibria always apply to

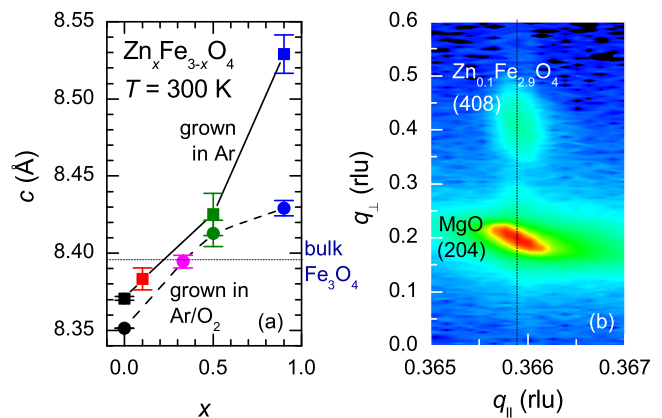


FIG. 3: (color online) (a) Change of the c axis lattice parameter of $\text{Zn}_x\text{Fe}_{3-x}\text{O}_4$ films grown on MgO(001) in pure Ar atmosphere (squares) and an Ar/O₂ mixture (circles) with Zn content x . The bulk c axis lattice constant of Fe_3O_4 is marked by the dashed horizontal line. (b) Reciprocal space map around the (204) reflection of the MgO(001) substrate. The (408) reflection from the $\text{Zn}_{0.1}\text{Fe}_{2.9}\text{O}_4$ film appears at the same in-plane scattering vector q_{\parallel} marked by the dashed vertical line.

thermal equilibrium situations which certainly are not appropriate for the laser-MBE growth process occurring far from equilibrium. Nevertheless, the high energy of the particles in the laser plume can be associated to an effective growth temperature much larger than the substrate temperature favoring the stability of Fe_3O_4 ^{24,25}. Therefore, for the deposition temperature and oxygen partial pressure used in our experiments we are sufficiently far away from the $\text{Fe}_3\text{O}_4/\gamma\text{-Fe}_2\text{O}_3$ equilibrium line^{37,38}.

As shown by Fig. 2, the (004) reflection from $\text{Zn}_x\text{Fe}_{3-x}\text{O}_4$ can be clearly observed together with satellites due to Laue oscillations. These oscillations demonstrate that the thin films are coherently strained and have a small surface roughness. The rocking curves of the (004) or (008) reflections (insets of Fig. 2) show a full width at half maximum (FWHM) of $\Delta\omega \leq 0.05^\circ$. This demonstrates the excellent structural quality of the $\text{Zn}_x\text{Fe}_{3-x}\text{O}_4$ thin film samples with very low mosaic spread, comparable to epitaxial Fe_3O_4 films^{33,35}. In the ω - 2θ scan, the (004) reflection from Fe_3O_4 is positioned at a slightly larger angle than the (002) reflection from the MgO substrate (see Fig. 2(a,b)), indicating $c_{\text{Fe}_3\text{O}_4} < 2c_{\text{MgO}}$. With increasing Zn concentration, the (004) reflection moves to lower angles and crosses the MgO(002) reflection at $x = 0.5$ (see Fig. 2(e,f)). At $x = 0.9$, the position of the (004) reflection from the $\text{Zn}_x\text{Fe}_{3-x}\text{O}_4$ film is shifted to an angle below the (002) reflection from MgO (see Fig. 2(g,h)). This corresponds to $c_{\text{Zn}_{0.9}\text{Fe}_{2.1}\text{O}_4} > 2c_{\text{MgO}}$.

The absolute value and variation of the c axis lattice parameter of the $\text{Zn}_x\text{Fe}_{3-x}\text{O}_4$ films with Zn content x are related to two effects, namely epitaxial coherency strain and the larger ionic radius of tetrahedrally coordinated

Zn^{2+} of 0.6 Å compared to the radius of only 0.49 Å of Fe^{3+} on the tetrahedrally coordinated A site¹². First, for $x = 0$ the lattice mismatch of -0.4% between Fe_3O_4 film and MgO substrate leads to a tensile in-plane epitaxial coherency strain and, in turn, to a slight reduction of the c axis lattice parameter of the Fe_3O_4 film below the bulk value (cf. Fig. 3(a)). The fully coherent growth of the $\text{Zn}_x\text{Fe}_{3-x}\text{O}_4$ thin films is demonstrated by reciprocal space maps around the (204) reflection of the MgO substrate (see Fig. 3(b)). The (408) reflection of the film is located exactly at the same in-plane scattering vector q_{\parallel} as the (204) reflection of the substrate. This clearly demonstrates that the in-plane lattice constant of the film perfectly matches twice the one of the MgO substrate. Second, for $x > 0$ the unit cell volume of $\text{Zn}_x\text{Fe}_{3-x}\text{O}_4$ is expected to increase about linearly with increasing x due to the larger ionic radius of Zn^{2+} . However, since the $\text{Zn}_x\text{Fe}_{3-x}\text{O}_4$ films grow coherently on the MgO(001) substrate without any relaxation up to the maximal thickness of 60 nm studied in our experiments, the in-plane lattice constant stays unchanged. Only the out-of-plane lattice constant is found to vary with increasing x . Depending on whether the in-plane strain is tensile or compressive, a reduction or expansion of the unit cell in $[00\ell]$ direction, respectively, is found (Fig. 3(a)), resulting in a tetragonal distortion of the cubic lattice. The c axis parameter increases from a value below ($x = 0$, tensile strain) to a value above the bulk value ($x \gtrsim 0.3$, compressive strain). The expansion of the out-of-plane lattice parameter with increasing x has been reported also for (111)-oriented films grown on $\text{Al}_2\text{O}_3(0001)$ substrates¹². However, we note that those films are relaxed due to the very large lattice mismatch of 8% between film and substrate. Therefore, both results cannot be compared directly.

An interesting result shown in Fig. 3 is the fact that the c axis lattice parameters of the $\text{Zn}_x\text{Fe}_{3-x}\text{O}_4$ films grown in pure Ar atmosphere are larger than those of the films grown in an Ar/ O_2 mixture and also show a slightly weaker increase with Zn content in the range $0 \leq x \leq 0.5$. This most likely is caused by the formation of Fe vacancies when growing the films in finite oxygen partial pressure^{20,23,24,25,26}. The presence of Fe vacancies can be viewed as an internal negative pressure effect leading to a reduced cell volume. The weaker increase of the c axis parameter for the films grown in Ar/ O_2 suggests a partial compensation of the Fe vacancies by Zn substitution. This is in agreement with the transport data discussed below. We note, however, that this result has to be considered with some care. The problem is that the close vicinity of film and substrate reflections in the ω - 2θ scans does not allow an unambiguous derivation of the film c axis parameter with small error bars.

In summary, the structural analysis demonstrates that our $\text{Zn}_x\text{Fe}_{3-x}\text{O}_4(001)$ thin films are coherently strained and show a very small mosaic spread. Zn substitution results in an increase of the unit cell volume, causing the in-plane epitaxial strain to change from tensile to com-

pressive on increasing the Zn content x . Growth in excess oxygen results in a reduction of the unit cell volume most likely due to the formation of Fe vacancies. The latter most likely are partially compensated by additional Zn substitution.

4. MAGNETOTRANSPORT PROPERTIES

For magnetite the electrical conduction above the Verwey transition is believed to be determined by the hopping of the spin-down electrons between the mixed-valent Fe_B^{2+} and Fe_B^{3+} ions on the B sublattice. From the hopping amplitude $t \sim 0.1$ eV an electron conduction bandwidth $D \sim 1$ eV is expected. However, experimental data cannot be explained within a simple band theory. They can be better ascribed to some thermally activated motion of charge carriers. The reason is that the bare hopping amplitude and bandwidth is strongly reduced due to the translation of a polaronic lattice deformation associated with electron motion^{39,40}. If the reduced bandwidth is smaller than the energy of polarization phonons (typically 70 meV in magnetite), small polaron hopping is expected⁴¹. We note that the hopping takes place between Fe_B^{2+} and Fe_B^{3+} ions on the B sublattice. Below the Curie temperature, the spins of these ions are aligned parallel in the ideal case. However, as discussed above in reality there is some spin canting on the B sublattice. This has to be taken into account by an appropriate spin correlation factor⁴² leading to a spin dependent part of the activation energy. Since the spin alignment is improved by applying a magnetic field, this spin-dependent part of the activation energy can be reduced by the external field resulting in a large negative magnetoresistance as shown below.

For magnetotransport measurements, the films were patterned into typically 45 μm wide and 350 μm long Hall bars directed in the $\langle 010 \rangle$ direction by photolithography and Ar ion beam milling⁴³. The longitudinal resistivity ρ_{xx} has been measured as a function of temperature T and applied magnetic field H using a standard four-probe technique. The films with $x = 0.9$ were found to be insulating and are not further discussed in the following. We note that measurements of the anomalous and the ordinary Hall effect have been reported previously^{35,44} and are not discussed here.

4.1. Temperature dependence of resistivity

The $\rho_{xx}(T)$ curves of representative samples with $x \leq 0.5$ are shown in Fig. 4. Despite a similar shape of all $\rho_{xx}(T)$ curves, it is evident that the absolute magnitude of ρ_{xx} sensitively depends on the Zn substitution x and the growth atmosphere. For both samples sets grown in pure Ar atmosphere and an Ar/ O_2 (99:1) mixture, $\rho_{xx}(T)$ increases by more than two orders of magnitude on decreasing T from 375 K down to 90 K. Plotting

$\log(\rho_{xx})$ on a reciprocal T scale as shown in Fig. 4(b) results in about linear curves over a wide temperature range except for the $x = 0$ and $x = 0.1$ samples grown in pure Ar atmosphere. The kink in $\rho_{xx}(T)$ of the $x = 0$ sample results from the Verwey transition discussed below. Fig. 4(b) suggests that the longitudinal resistivity of the samples with $x \gtrsim 0.1$ follows a simple activated behavior $\rho_{xx}(T) \propto \exp(E_a/k_B T)$ with the Boltzmann constant $k_B = 1.38 \times 10^{-23}$ J/K and activation energies E_a ranging between 61 and 84 meV. However, an unambiguous determination of the detailed transport process is difficult. As indicated by Fig. 4(c), the $\rho_{xx}(T)$ data also can be equally well fitted by small polaron hopping^{41,45,46}, $\rho_{xx}(T) \propto T \exp(E_{\text{pol}}/k_B T)$, with the potential barrier for polaron hopping, E_{pol} , ranging between 64 and 95 meV. Actually, small polaron hopping yields a slightly better fit for the samples grown in pure Ar atmosphere, whereas the simple activated transport better fits the transport data of the samples grown in an Ar/O₂ mixture. The derived activation energies are typical for zinc ferrites^{20,37,46,47,48}. We also note that a similar transport behavior with similar activation energies is reported for the mixed-valent manganites, where charge transport is determined by the hopping between mixed-valent Mn³⁺ and Mn⁴⁺ ions^{49,50,51,52}.

We next discuss the observability of the *Verwey*⁵³ transition in the measured $\rho_{xx}(T)$ curves. In bulk material, this metal-insulator transition, associated with a cubic to monoclinic structural phase transition, occurs at $T_V = 123$ K and in the classic picture is argued to arise from a charge ordering of the Fe_B²⁺ and Fe_B³⁺ on the B sublattice in a process reminiscent to Wigner crystallization⁵⁴. Whereas at $T > T_V$ the extra electrons from Fe_B²⁺ ions can hop to neighboring Fe_B³⁺ ions on the corner sharing tetrahedral network on the B sublattice, giving rise to electrical conduction, this process is frozen in at $T < T_V$ due to Coulomb repulsion⁵⁵. However, more recently it became evident that also elastic and orbital interactions play a significant role. This leads to a renewed controversial discussion of the nature of the Verwey transition^{18,56,57,58,59}. It is evident from Fig. 4 that a pronounced change in the $\rho_{xx}(T)$ curves due to the Verwey transition is observed only for the Fe₃O₄ film ($x = 0$) grown in pure Ar atmosphere. For this film there is no jump but a clear kink in the $\rho_{xx}(T)$ curve at a slightly reduced temperature of about 115 K. For all other samples no clear signature of the Verwey transition is observable. This can be understood in a straightforward way. As discussed above, both substitution of Zn and introducing Fe vacancies by growing the films in finite oxygen partial pressure results in deviations from equal numbers of Fe_B²⁺ and Fe_B³⁺ on the B sublattice. This can be viewed as disorder on the B sublattice, tending to smear out the Verwey transition. The fact that the observability of the Verwey transition seems to sensitively depend on deviations from perfect stoichiometry already has been reported in literature^{20,23,25,26,28} and is further supported by our results. The other way round, we can

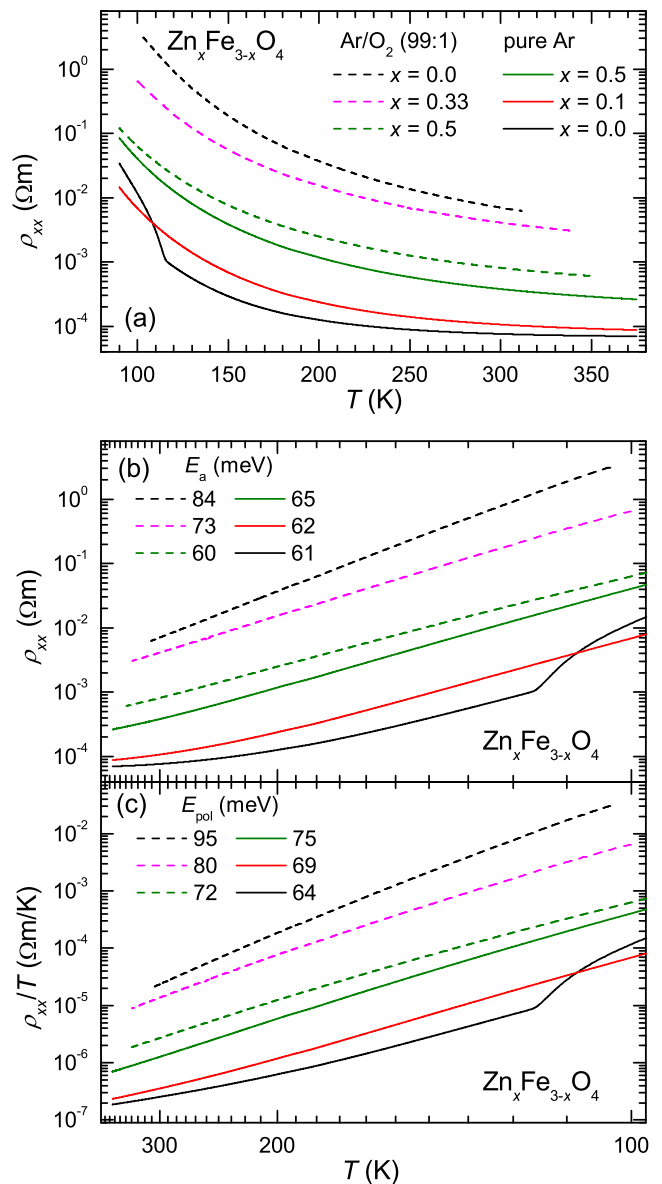


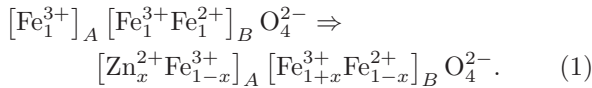
FIG. 4: (color online) (a) Longitudinal resistivity ρ_{xx} as a function of temperature T for epitaxial $\text{Zn}_x\text{Fe}_{3-x}\text{O}_4$ thin films, grown in pure Ar atmosphere (solid lines) or an Ar/O₂ (99:1) mixture (dashed lines) on MgO(001) substrates. In (b) and (c) ρ_{xx} and ρ_{xx}/T of the same samples are plotted versus a reciprocal temperature scale. Fitting the linear parts of the curves in (b) and (c) by $\rho_{xx} \propto \exp(E_a/k_B T)$ and $\rho_{xx}/T \propto \exp(E_{\text{pol}}/k_B T)$, respectively, gives the listed activation energies E_a and E_{pol} .

argue that the absence of any clear signature of the Verwey transition for the Fe₃O₄ films substituted by Zn or grown in finite oxygen partial pressure provides evidence for the presence of an unequal number of Fe_B²⁺ and Fe_B³⁺ ions on the B sublattice.

We next discuss the ρ_{xx} values of the $\text{Zn}_x\text{Fe}_{3-x}\text{O}_4$ ($0 \leq x \leq 0.5$) films grown in pure Ar atmosphere. The strong increase of resistivity with decreasing T can be un-

derstood in terms of a thermally activated hopping type transport mechanism of the itinerant electrons on the B sublattice. For $x = 0$, the room temperature ρ_{xx} value ($7.6 \times 10^{-5} \Omega\text{m}$) corresponds well with literature data for Fe_3O_4 thin films³⁵ or single crystals⁶⁰. In this context, we note that the presence of anti-phase boundaries (APBs) in Fe_3O_4 thin film samples may have a significant influence on the measured longitudinal resistivity⁶¹. However, this is not the case for our samples. First, our Fe_3O_4 thin film grown in Ar atmosphere has a room-temperature resistivity value close to that of Fe_3O_4 single crystals ($6.2 \times 10^{-5} \Omega\text{m}$) considered as APB-free⁶⁰. Second, comparing the resistivity value to those of Fe_3O_4 thin films with different APB density, we estimate that the volume fraction of the APB phase in our thin film is less than 20%⁶¹. Third, it is known that the formation and the density of APBs sensitively depends on the used substrates⁶² or the film thickness⁶¹. However, in our study always the same substrate and film thickness is used. Since also Zn substitution is not expected to severely affect the APB density, we can safely assume that all samples grown in the same atmosphere have a similar APB density.

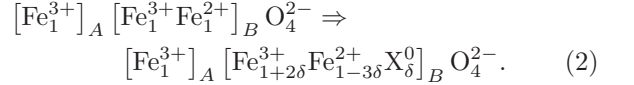
With increasing x , as discussed in the introduction, Zn^{2+} preferably occupies the tetrahedrally coordinated A site in the inverse spinel structure²¹. Hence, the substitution of Fe_A^{3+} by Zn^{2+} reduces the amount of Fe_B^{2+} as



That is, the density of itinerant electrons on the B sublattice is reduced, resulting in an increase of the resistivity with increasing x . This is in perfect agreement with our observation and literature data^{12,13}. We note however, that the increase of resistivity is not only caused by a reduction of the carrier density but also by several other effects. First, deviations from the 1:1 balance of Fe_B^{2+} and Fe_B^{3+} on the B sublattice causes disorder, tending to localize the itinerant charge carriers. Second, Zn substitution dilutes the A sublattice, thereby weakening the antiferromagnetic exchange J_{AB} between the A and B sublattices. As discussed above, this results in spin canting on the B sublattice, reducing the hopping amplitude. This amplitude is maximum for a parallel alignment of the local moments due to strong antiparallel Hund's rule coupling of the spins of the itinerant electrons. Both effects are expected to result in an increase of the activation energy for the hopping transport with increasing x in agreement with our observations.

The $\rho_{xx}(T)$ curves of the $\text{Zn}_x\text{Fe}_{3-x}\text{O}_4$ ($0 \leq x \leq 0.5$) films grown in an Ar/ O_2 mixture show a similar overall temperature dependence, however, with resistivity values that are much higher than those measured for the films grown in pure Ar atmosphere. Furthermore, the resistivity values decrease with increasing x in contrast to what is observed for the films grown in Ar. We first

discuss the origin of the much higher resistivity value ($\rho_{xx} = 7 \times 10^{-3} \Omega\text{m}$ at 300 K) of the Fe_3O_4 ($x = 0$) film grown in finite oxygen partial pressure compared to that ($\rho_{xx} = 7.6 \times 10^{-5} \Omega\text{m}$ at 300 K) of the film grown in pure Ar. Since growth of magnetite in excess oxygen is known to create Fe vacancies $\text{X}^{0,23,24,25,26}$, equivalent to two (three) missing electrons per Fe^{2+} (Fe^{3+}) vacancy, the requirement of charge neutrality shifts the 1:1 balance between Fe_B^{2+} and Fe_B^{3+} towards Fe_B^{3+} as



Evidently, Fe vacancies in the same way as Zn substitution result in a reduction of Fe_B^{2+} . Hence, the density of itinerant electrons on the B sublattice decreases and, in turn, the resistivity increases with increasing δ . This is exactly what is observed in our experiments and reported in literature^{20,63}. Actually, for $\text{Zn}_x\text{Fe}_{3-x}\text{O}_4$ ($0 \leq x \leq 0.3$) single crystals Wang *et al.* report a compositional correspondence $x \approx 3\delta$ regarding the measured resistivity data²⁰. Again, with the same arguments given above for the films grown in pure Ar, a reliable evaluation of the various mechanisms (localization, spin canting) responsible for the increase in resistivity is not possible. We also note that according to eq.(2) growth in high oxygen partial pressure (not the case in our experiments) may lead to the formation of the cubic $\gamma\text{-Fe}_2\text{O}_3$ (maghemite) phase in the extreme case of $\delta = 1/3$ ⁶⁴.

Zn substitution in our magnetite films grown in an Ar/ O_2 mixture results in a decrease of resistivity in contrast to what is observed for the films grown in pure Ar atmosphere. On first sight, this is astonishing and seems to be in conflict with the above discussion, since Zn^{2+} again preferably occupies the tetrahedrally coordinated A lattice sites²¹, substituting Fe^{3+} and thereby reducing carrier density. That is, one would expect an increase of resistivity with increasing x . However, since Zn substitution also results in an increase of the unit cell volume due to the larger ionic radius of Zn^{2+} compared to Fe^{3+} , it is expected that Zn substitution removes part of the Fe vacancies. This is intuitive since now Fe can be more easily incorporated into the expanded lattice. Then, it is expected that Zn^{2+} does not only remove an electron by substituting Fe_A^{3+} on an A site, but also adds two/three electrons by removing a vacancy on a $\text{Fe}_B^{2+}/\text{Fe}_B^{3+}$ site. That is, by Zn substitution also X^0 is replaced by Fe^{2+} or Fe^{3+} . Evidently, in total this leads to an effective increase of the carrier density with increasing x in agreement with our experimental data in the range up to $x = 0.5$. The partial removal of the Fe vacancies by Zn substitution is in agreement with the x-ray data of Fig. 3(a).

In summary, the $\rho_{xx}(T)$ curves of the $\text{Zn}_x\text{Fe}_{3-x}\text{O}_4$ films grown under different oxygen partial pressure show a similar shape, originating from a hopping type transport mechanism, but strongly differing absolute resistivity values. These differences can be consistently explained by the change of the itinerant charge carrier density on the B sublattice and their hopping amplitude by

either Zn substitution or the generation of Fe vacancies due to growth at finite oxygen partial pressure. However, applying both Zn substitution and excess oxygen results in an increase of the carrier density as Zn substitution is removing part of the Fe vacancies generated by excess oxygen. It would be interesting to directly check the change of the carrier density by measurements of the Hall effect. However, we cannot unambiguously separate the small ordinary from the large anomalous Hall contribution and any attempt to do so would result in large errors of the derived carrier density⁴⁴.

We note that the observed dependence of the resistivities on the Zn substitution levels x cannot be simply explained by the assumption of different APB densities in the different thin film samples. It is unlikely that with increasing x the APB density increases for samples of the same thickness when grown in Ar atmosphere while it decreases for those prepared in the Ar/O₂ mixture. Moreover, the samples show a universal scaling relation of the anomalous Hall conductivity with the longitudinal conductivity indicating a negligibly small APB resistivity as already pointed out earlier⁴⁴.

4.2. Magnetoresistance

In this subsection we address the magnetoresistance (MR) of the $\text{Zn}_x\text{Fe}_{3-x}\text{O}_4$ films. The MR effect, $\text{MR}_{xx} = [\rho_{xx}(H) - \rho_{xx}(0)]/\rho_{xx}(0)$ is shown in Fig. 5(a) at several temperatures for the $x = 0.1$ samples grown in pure Ar. As shown in Fig. 5(b), very similar $\text{MR}_{xx}(H)$ curves with similar absolute values of MR_{xx} at room temperature are found for the other samples, although the absolute values of their resistivities vary by more than two orders of magnitude (cf. Fig. 4). This interesting observation can be consistently explained in the framework of thermally activated hopping of the itinerant electrons on the B sublattice. Due to the strong on-site Hund's rule coupling, the spins of the itinerant spin-down electrons are coupled antiparallel to the localized spins formed by the spin-up electrons. Therefore, the activation energy for the hopping process is given by the sum of a spin independent energy (E_a or E_{pol}) and a spin dependent contribution E_s . The latter depends on the spin canting of the local moments on the B sublattice and disappears for a perfect parallel alignment. Since in the presence of a finite canting of the local moments an applied magnetic field tends to improve the alignment, a magnetic field dependent total activation energy $E(H) = E_{a,\text{pol}} + E_s(H)$ is obtained. Then, no matter whether the transport is by thermally activated hopping, $\rho_{xx} = \rho_{0,a} \exp[E(H)/k_B T]$, or small polaron hopping, $\rho_{xx}/T = \rho_{0,\text{pol}} \exp[E(H)/k_B T]$,

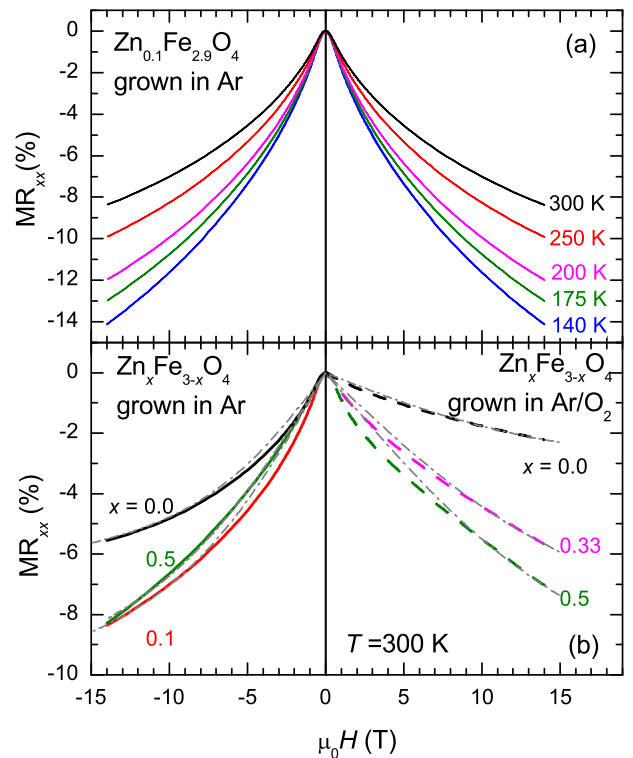


FIG. 5: (color online) (a) MR_{xx} plotted versus the magnetic field H applied perpendicular to the film plane at different temperatures for $\text{Zn}_{0.1}\text{Fe}_{2.9}\text{O}_4$ thin films grown in pure Ar atmosphere. (b) $\text{MR}_{xx}(H)$ curves measured at 300 K for different $\text{Zn}_x\text{Fe}_{3-x}\text{O}_4$ grown in pure Ar atmosphere (left) or an Ar/O₂ mixture (right). The dash-dotted gray lines are fits to the data according to eq.(6).

the MR effect is obtained as

$$\begin{aligned} \text{MR}_{xx} &= \frac{\exp\left(\frac{E_s(H)}{k_B T}\right) - \exp\left(\frac{E_s(0)}{k_B T}\right)}{\exp\left(\frac{E_s(0)}{k_B T}\right)} \\ &= \exp\left(\frac{-\Delta E_s(H)}{k_B T}\right) - 1. \end{aligned} \quad (3)$$

with $\Delta E_s(H) = E_s(0) - E_s(H)$. Evidently, with the assumptions made, $\text{MR}_{xx}(H)$ is independent of the magnitude of the prefactors ($\rho_{0,a}$ or $\rho_{0,\text{pol}}$) and the activation energies (E_a or E_{pol}), which may strongly vary for samples with different x and grown in different atmosphere. Moreover, similar $\text{MR}_{xx}(H)$ curves with comparable absolute values are obtained, if the magnetic field induced change $\Delta E_s(H)$ of the spin-dependent part of the activation energy is about the same for all samples.

Since the transport in $\text{Zn}_x\text{Fe}_{3-x}\text{O}_4$ by hopping of the t_{2g} spin-down electrons between mixed-valent $\text{Fe}_B^{2+}/\text{Fe}_B^{3+}$ ions is equivalent to the hopping of the e_g electrons between mixed-valent $\text{Mn}^{3+}/\text{Mn}^{4+}$ ions in the doped manganites, we can adopt models developed for the MR effect in the perovskite manganites^{65,66,67}. According to these models the magnetic field dependent change of the acti-

vation energy for hopping between two lattice sites i and j can be expressed as

$$\Delta E_s(H) = \alpha (\langle \mathbf{m}_i \cdot \mathbf{m}_j \rangle_H - \langle \mathbf{m}_i \cdot \mathbf{m}_j \rangle_{H=0}), \quad (4)$$

where \mathbf{m}_i and \mathbf{m}_j are the local moments on the lattice sites i and j , $\langle \dots \rangle_{H=0}$ and $\langle \dots \rangle_H$ denote the sample average at zero and finite magnetic fields, respectively, and α is a constant that may depend on temperature. The local moments \mathbf{m}_i and \mathbf{m}_j can be associated either with the localized spins of the individual Fe ions or the moments of small spin clusters. Note that these spin clusters also can be considered as spin polarons, that is, itinerant electrons dressed by a small cloud of parallel aligned localized spins. Evidently, $\Delta E_s = 0$ is independent of H , if the local moments are already perfectly aligned in zero magnetic field (ideal ferromagnet). In this case, no MR effect is expected. However, if there is a finite canting of the neighboring moments, applying a magnetic field results in a reduction of this spin canting and thereby in $\Delta E_s > 0$. According to eq.(3) this results in a finite negative MR effect with a magnitude determined by the value of $\Delta E_s/k_B T$. The magnetic field dependence of ΔE_s can be estimated by keeping in mind that in the ferromagnetic state both the molecular field and the applied magnetic field support a parallel alignment of the local moments. Since the molecular field is usually much larger than the applied field, the deviations of the directions of the local moments from the average direction are small. In this case $\Delta E_s(H)$ is found to follow the Brillouin function \mathfrak{B} giving^{65,66,67}

$$\Delta E_s(H) = \beta \mathfrak{B} \left(\frac{\mu_{\text{eff}} \mu_0 H}{k_B T} \right). \quad (5)$$

with the vacuum permeability $\mu_0 = 4\pi \times 10^{-7}$ Vs/Am. Here, μ_{eff} is the average value of the local moments and β a constant, which may show a weak temperature dependence. Assuming $\Delta E_s \ll k_B T$, what certainly is a reasonable assumption at room temperature, we can approximate eq.(3) by

$$\text{MR}_{xx} \simeq -\beta \frac{\mathfrak{B} \left(\frac{\mu_{\text{eff}} \mu_0 H}{k_B T} \right)}{k_B T}. \quad (6)$$

This shows that the magnetic field dependence of the MR effect measured at constant temperature should follow the Brillouin function. As shown in Fig. 5(b), this is indeed the case. The data of all samples can be well fitted by eq.(6). Fitting the data gives the μ_{eff} values of the local moments. They range between 70 to 120 μ_B and 60 to 70 μ_B , corresponding to about 18 to 30 and 15 to 18 Fe^{2+} ions, for the samples grown in pure Ar and an Ar/O₂ mixture, respectively. Here, μ_B is Bohr's magneton. Evidently, the derived moments are larger than the localized spins of the individual Fe ions. They can be considered as the moments of small ferromagnetic clusters with perfectly parallel spins, in which the electrons can move freely, but with small misalignment between

neighboring clusters. Since there are eight Fe^{2+} ions per unit cell, their size ranges between about two and four unit cells. We also note that eq.(6) does not only describe the magnetic field dependence of the MR effect but also nicely explains the decrease of the MR effect with increasing temperature.

In summary, the MR effect of the $\text{Zn}_x\text{Fe}_{3-x}\text{O}_4$ films in the same way as the $\rho_{xx}(T)$ data can be well described within a model based on thermally activated hopping of itinerant charge carriers or small polarons between the mixed-valent $\text{Fe}_B^{2+}/\text{Fe}_B^{3+}$ ions on the B sublattice. The activation energy contains a magnetic field dependent part, which depends on the misalignment of the neighboring spin moments. Within this model, $\text{MR}_{xx} \propto -\mathfrak{B}(\text{const. } H/T)$ is expected in good agreement with the experimental data. In particular, the similar $\text{MR}_{xx}(H)$ curves for samples with strongly different ρ_{xx} values and the decrease of the MR effect with increasing temperature are nicely reproduced.

5. MAGNETIC PROPERTIES

We have seen that Zn substitution and the creation of Fe vacancies in magnetite results in changes of the carrier density and hopping amplitudes of the itinerant charge carriers on the B sublattice. Following our discussion in the introduction, this is expected to have significant influence on the magnetic properties. Therefore, we also systematically analyzed the magnetic properties of the $\text{Zn}_x\text{Fe}_{3-x}\text{O}_4$ films. The magnetic characterization was performed with the unpatterned films using SQUID magnetometry with magnetic fields $\mu_0 H$ up to 7 T applied in the film plane. At room temperature, the $M(H)$ loops show ferromagnetic behavior for all samples (Fig. 6). However, the measured saturation magnetization M_S as well as the remanent magnetization M_R and coercive field was found to strongly depend on both the Zn substitution level x and the growth atmosphere.

We start our discussion with the stoichiometric Fe_3O_4 film grown in pure Ar atmosphere, serving as a reference. Figure 6(a) shows that for this film the highest values for the room temperature saturation magnetization ($M_S = 3.16 \mu_B/\text{f.u.}$) and remanence ($M_R = 1.83 \mu_B/\text{f.u.}$) are obtained. We note that we do not obtain the theoretically expected value of $M_S = 4 \mu_B/\text{f.u.}$ This is typical for thin film samples due to the presence of APBs^{28,29}. However, the value measured for our film is among the highest reported in literature and corresponds well with the volume fraction of the APB phase of 20% estimated above.

We next discuss the evolution of the saturation magnetization of the $\text{Zn}_x\text{Fe}_{3-x}\text{O}_4$ films grown in pure Ar atmosphere with increasing x . As shown in the inset of Fig. 6(a), both M_S and M_R were found to decrease with increasing x . Recalling eq.(1), the substitution of Fe_A^{3+} ($3d^5, S = 5/2$) by Zn^{2+} ($3d^{10}, S = 0$) results in a decrease of the magnetization on the A sublattice. That

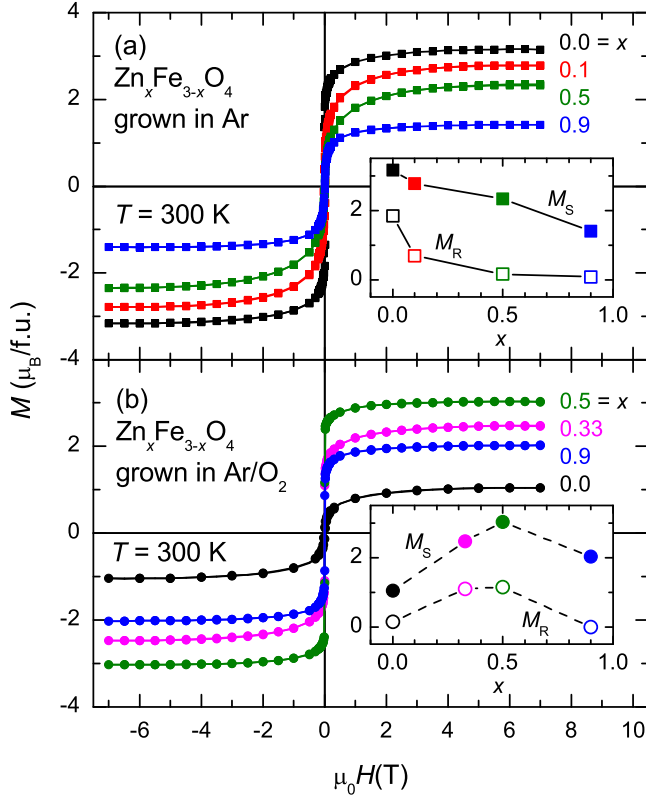


FIG. 6: (color online) Room temperature magnetization M versus magnetic field H applied in the film plane for $\text{Zn}_x\text{Fe}_{3-x}\text{O}_4$ thin films grown in (a) pure Ar atmosphere and (b) in an Ar/ O_2 (99:1) mixture. The insets show the saturation magnetization M_S (full symbols) and the remanence M_R (open symbols) in units of $\mu_B/\text{f.u.}$ as a function of the Zn substitution level x . The lines are guides to the eye.

is, since the compensating magnetization of the A sublattice is removed, one would expect an increase of the total magnetization of the ferrimagnet. However, Zn substitution also weakens J_{AB} by diluting the A site moments. Furthermore, it converts Fe_B^{2+} ($3d^6, S = 2$) into Fe_B^{3+} on the B sublattice, resulting in a reduction of the itinerant charge carrier density. This weakens the ferromagnetic double exchange, competing with antiferromagnetic superexchange interaction on the B sublattice. As discussed in the introduction, taken together this leads to an increase of the spin canting on the B sublattice with increasing x (cf. Fig. 1), explaining the observed reduction of the total magnetization of the ferrimagnetic $\text{Zn}_x\text{Fe}_{3-x}\text{O}_4$ films. We note that recently Takaobushi *et al.* reported a monotonic increase of the saturation magnetization from about $0.5 \mu_B/\text{f.u.}$ to $3.2 \mu_B/\text{f.u.}$ at 10 K in the range $0 \leq x \leq 0.9$ and explained this observation by the assumption that the A sublattice magnetization is reduced by Zn substitution¹². Comparison of the low temperature saturation magnetization of the $x = 0$ films ($3.31 \mu_B/\text{f.u.}$ when grown in Ar in our case, $0.5 \mu_B/\text{f.u.}$ in Ref.¹²) clearly shows that the samples can-

not be directly compared. The reason is that the films in Ref.¹² have been grown at finite oxygen partial pressure of 1.0×10^{-6} mbar. In this case, the effect of Fe vacancies has to be taken into consideration as follows.

The magnetic properties of the $\text{Zn}_x\text{Fe}_{3-x}\text{O}_4$ films grown in an Ar/ O_2 (99:1) mixture are shown in Fig. 6(b). There are pronounced differences to the films grown in pure Ar atmosphere. First, for $x = 0$ both M_S and M_R are much lower than for the films grown in pure Ar. Second, M_S and M_R is found to increase with increasing x for $0 \leq x \leq 0.5$ and then to decrease again for $x = 0.9$ as shown in the inset of Fig. 6(b). The coercive field decreases from about 55 mT to 8 mT on increasing x from 0 to 0.9. The $M_S(x)$ dependence can be straightforwardly explained by the presence of Fe vacancies in films grown in finite oxygen partial pressure and their removal by Zn substitution. For $x = 0$, the Fe vacancies shift the $\text{Fe}_B^{2+}/\text{Fe}_B^{3+}$ 1:1 balance towards Fe_B^{3+} , removing itinerant charge carriers and weakening the ferromagnetic double exchange at the expense of antiferromagnetic superexchange on the B sublattice. This results in spin canting on the B sublattice, giving rise to a reduced saturation magnetization. On Zn substitution, part of the Fe vacancies are removed. This shifts the $\text{Fe}_B^{2+}/\text{Fe}_B^{3+}$ ratio back towards a 1:1 balance. The related increase of the itinerant charge carrier density and DE interaction on the B sublattice reduces the spin canting with increasing x . This explains the increase of the room temperature saturation magnetization in the range $0 < x \leq 0.5$ from $M_S = 1.05 \mu_B/\text{f.u.}$ up to $3.02 \mu_B/\text{f.u.}$ at $x = 0.5$. At 10 K, M_S increases from $1.26 \mu_B/\text{f.u.}$ at $x = 0$ up to $3.92 \mu_B/\text{f.u.}$ at $x = 0.5$. For even larger x , the Fe_A^{3+} moments on the A sublattice are strongly diluted, resulting in a strong weakening of the antiferromagnetic

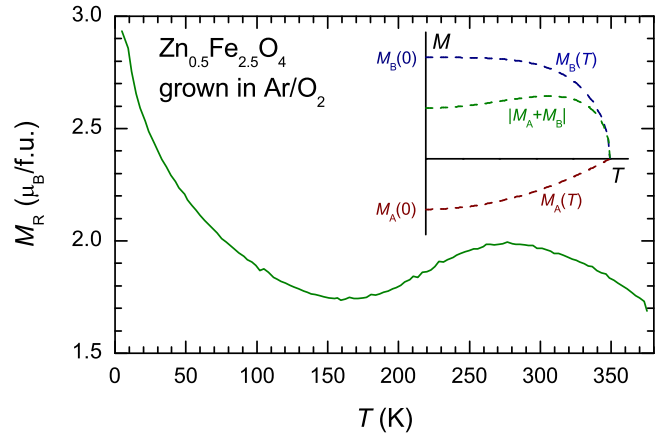


FIG. 7: (color online) Remanent magnetization M_R plotted versus temperature T for a $\text{Zn}_{0.5}\text{Fe}_{2.5}\text{O}_4$ film grown in an Ar/ O_2 (99:1) mixture. The data were taken after field cooling at 7 T on increasing the temperature at zero applied magnetic field. The inset schematically shows the hump in the $M(T)$ curve as the result of two opposite sublattice magnetizations with different T dependence.

superexchange J_{AB} between the A and B sublattices. Furthermore, Zn substitution may overcompensate the Fe vacancies again shifting the $\text{Fe}_B^{2+}/\text{Fe}_B^{3+}$ balance towards Fe_B^{3+} . Taken together, this explains the decrease of M_S above the critical value of $x \approx 0.5$, which of course depends on the oxygen partial pressure during growth and the corresponding amount of Fe vacancies. The observed increase of M_S with increasing x for $\text{Zn}_x\text{Fe}_{3-x}\text{O}_4$ films grown in an Ar/ O_2 mixture is consistent with the result of Takaobushi *et al.*¹², who reported an increase of $M_S(10\text{ K})$ from $0.5 \mu_B/\text{f.u.}$ to $3.2 \mu_B/\text{f.u.}$ on increasing x from 0 to even 0.9. However, our systematic study strongly suggests that this increase is most likely caused by the removal of Fe vacancies rather than due to the removal of Fe_A^{3+} moments on the A sites as argued in Ref.¹².

Figure 7 shows the temperature dependence of the remanent magnetization M_R for a $\text{Zn}_{0.5}\text{Fe}_{2.5}\text{O}_4$ film grown in an Ar/ O_2 mixture. In agreement with the $\rho_{xx}(T)$ data of Fig. 4, there is no indication for the *Verwey* transition in $M_R(T)$ around 120 K. This is the case for all samples, except for the Fe_3O_4 film grown in pure Ar. This observation is not only consistent with our transport data but also with magnetization data from other groups, indicating a smearing or suppression of the *Verwey* transition by an amount of Zn substitution as small as $x = 0.01$ ⁶⁸. As shown in Fig. 7, the measured $M_R(T)$ curve first decreases with increasing T , goes through a minimum at $T \approx 150\text{ K}$, then increases up to $T \approx 275\text{ K}$, before it decreases again towards room temperature. Such a behavior is often observed in ferrimagnets and can be explained on the basis of Néel's two sublattice model⁶⁹. Within this model the origin of the hump at 275 K is a different T dependence of the two sublattice magnetizations $M_A(T)$ and $M_B(T)$ due to different effective molecular fields on the A and B sites. In our case the effective molecular field on the A sublattice is expected to be smaller due to the partial substitution of Fe_A^{3+} by non-magnetic Zn^{2+} . As a result, the combined magnetization $M(T) = M_A(T) + M_B(T)$ should show an upward hump in agreement with the experimental result. Note that the observation of a hump, which is directed upwards, provides direct experimental evidence for A site substitution of Zn^{2+} in the inverse spinel structure⁶⁹. For the $x = 0.33$ sample, no hump could be observed, most likely due to a too small imbalance in the effective molecular fields at the smaller substitution level.

In conclusion, the magnetic properties of the $\text{Zn}_x\text{Fe}_{3-x}\text{O}_4$ films grown under different oxygen partial pressure strongly depend on whether the films were grown in pure Ar atmosphere or at finite oxygen partial pressure. Fully consistent with the transport data these differences can be explained by the following effects: (i) For films grown in pure Ar, Zn substitution on the A site removes Fe_A^{3+} moments from the A sublattice and due to charge neutrality itinerant electrons from the B sublattice. The resulting weakening of both the antiferromagnetic A - O - B SE and the ferromagnetic DE

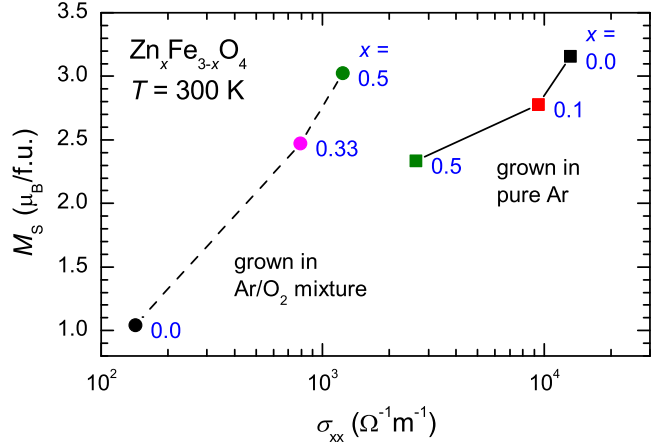


FIG. 8: (color online) Saturation magnetization M_S plotted versus the longitudinal conductivity σ_{xx} for epitaxial $\text{Zn}_x\text{Fe}_{3-x}\text{O}_4$ thin films with different Zn substitution $x \leq 0.5$ grown in pure Ar atmosphere (squares) or an Ar/ O_2 (99:1) mixture (circles).

on the B sublattice results in an increasing spin canting on the B sublattice with increasing x . This causes a reduction of the saturation magnetization with increasing x . (ii) For films grown in oxygen partial pressure, the magnetic properties are strongly influenced by the presence of Fe vacancies. They reduce the density of itinerant electrons on the B sublattice thereby weakening the ferromagnetic DE at the expense of antiferromagnetic SE. This causes spin canting on the B sublattice and, in turn, a reduced saturation magnetization. The effect of additional Zn substitution is the partial removal of the Fe vacancies. This effectively increases the density of itinerant electrons on the B sublattice thereby strengthening the ferromagnetic DE. The result is an increase of the saturation magnetization with increasing x . Again, the observed dependence of the saturation magnetization on the Zn substitution levels x cannot be simply explained by different APB densities in the different thin film samples. It is very unlikely that the APB density increases with increasing x for samples of the same thickness when grown in Ar atmosphere while for those prepared in the Ar/ O_2 mixture it first decreases for $x \leq 0.5$ and then increases again for $x \geq 0.5$.

We finally link the magnetic properties to the transport data by plotting the saturation magnetization M_S versus the electrical conductivity $\sigma_{xx} \simeq 1/\rho_{xx}$ ⁴⁴ for films with various x and grown in Ar or Ar/ O_2 (Fig. 8). Evidently, there is a clear correlation between M_S and σ_{xx} . Samples with high M_S have large σ_{xx} and vice versa. Again, this correlation can be straightforwardly explained within the scenario presented above. Charge transport is dominated by the hopping of the itinerant t_{2g} electrons between the mixed-valent $\text{Fe}_B^{2+}/\text{Fe}_B^{3+}$ ions on the B sublattice. Due to the strong on-site Hund's rule coupling the spin of the hopping spin-down electron is aligned anti-parallel to the

local moment of the spin-up electrons (cf. Fig. 1). Therefore, the hopping amplitude is significantly suppressed if the moments of neighboring B sites are not parallel. That is, any spin canting on the B sublattice reducing the saturation magnetization also results in a reduction of the electrical conductivity.

6. CONCLUSION

We have grown epitaxial $\text{Zn}_x\text{Fe}_{3-x}\text{O}_4$ thin films ($0 \leq x \leq 0.9$) with excellent structural properties both in pure Ar atmosphere and an Ar/O₂ mixture using laser molecular beam epitaxy. We show that the electrical conductivity and the saturation magnetization can be tuned over a wide range ($1.0 \dots 3.2 \mu\text{B}/\text{f.u.}$ and $10^2 \dots 10^4 \Omega^{-1}\text{m}^{-1}$ at room temperature) by Zn substitution and/or finite oxygen partial pressure during growth. This demonstrates that $\text{Zn}_x\text{Fe}_{3-x}\text{O}_4$ can be used as a material with tailored electrical and magnetic properties. Our comprehensive study shows that electrical conduction, magnetotransport, and the magnetic properties of $\text{Zn}_x\text{Fe}_{3-x}\text{O}_4$ are dominated by the density and thermally activated hopping of the itinerant t_{2g} electrons between the mixed-valent $\text{Fe}_B^{2+}/\text{Fe}_B^{3+}$ ions, providing electrical conduction and mediating a ferromagnetic DE interaction on the B sublattice. This scenario is confirmed by the observation that the saturation magnetization scales with the longitudinal conductivity and the field dependence of the MR effect. Our combined systematic analysis of the magnetotransport and magnetic properties also provides a clear picture of the effect of Zn substitution and growth in finite oxygen partial pressure. First, Zn substitution

removes both Fe_A^{3+} moments from the A sublattice and itinerant charge carriers from the B sublattice. Second, growth in finite oxygen partial pressure generates Fe vacancies, also removing itinerant charge carriers from the B sublattice. Hence, in both cases a reduction of the charge carrier density and a weakening of the ferromagnetic DE on the B sublattice is obtained. This results in an increase of resistivity and a reduction of the saturation magnetization due to spin canting on the B sublattice. Third, applying both Zn substitution and growth in oxygen at the same time does not result in an additive effect. In contrast, a compensation effect is observed, since Zn substitution removes part of the Fe vacancies. To sum up, one can say that the high Curie temperature together with the electrical and magnetic properties that can be tuned over a wide range make $\text{Zn}_x\text{Fe}_{3-x}\text{O}_4$ a promising functional material for spintronic devices. The combination of $\text{Zn}_x\text{Fe}_{3-x}\text{O}_4$ with semiconductor materials such as ZnO in multi-functional heterostructures²⁷ will be particularly appealing.

Acknowledgments

We thank Andreas Erb for the preparation of polycrystalline target materials for the laser-MBE process and Thomas Brenninger for continuous technical support. Financial support by the German Science Foundation within the priority programs 1157 and 1285 (project Nos. GR 1132/13 & 14) and the German Excellence Initiative via the *Nanosystems Initiative Munich (NIM)* is gratefully acknowledged. D.V. and M.S.R.R. thank the DAAD for financial support.

* Electronic address: Matthias.Opel@wmi.badw.de

† Electronic address: Rudolf.Gross@wmi.badw.de

¹ S.A. Wolf, D. D. Awschalom, R. A. Buhrman, J. M. Daughton, S. von Molnar, M. L. Roukes, A. Y. Chtchelkanova, and D. M. Treger, *Science* **294**, 1488 (2001).

² I. Zutic, J. Fabian, S. Das Sarma, *Rev. Mod. Phys.* **76**, 323 (2004).

³ J. S. Moodera, L. R. Kinder, T. M. Wong, R. Meservey, *Phys. Rev. Lett.* **74**, 3273 (1995).

⁴ H. Ohno, D. Chiba, F. Matsukura, T. Omiya, E. Abe, T. Dietl, Y. Ohno, and K. Ohtani, *Nature* **408**, 944 (2000).

⁵ D. Chiba, M. Yamanouchi, F. Matsukura, and H. Ohno, *Science* **301**, 943 (2003).

⁶ S.T.B. Goennenwein, M. Althammer, C. Bihler, A. Brandlmaier, S. Geprägs, M. Opel, R. Gross, W. Schoch, W. Limmer, H. Huebl, and M. S. Brandt, *phys. stat. sol. (RRL)* **2**, 96 (2008).

⁷ C. Bihler, M. Althammer, A. Brandlmaier, S. Geprägs, M. Weiler, M. Opel, W. Schoch, W. Limmer, R. Gross, M. S. Brandt, and S.T.B. Goennenwein, *Phys. Rev. B* **78**, 045203 (2008).

⁸ H. Tanaka, J. Zhang, and T. Kawai, *Phys. Rev. Lett.* **88**, 027204 (2001).

⁹ Z. Zhang and S. Satpathy, *Phys. Rev. B* **44**, 13319 (1991).

¹⁰ Y. S. Dedkov, U. Rüdiger, and G. Güntherodt, *Phys. Rev. B* **65**, 064417 (2002).

¹¹ M. Fonin, Y. S. Dedkov, R. Pentcheva, U. Rüdiger and G. Güntherodt, *J. Phys.: Condens. Matter* **19**, 315217 (2007); see also *J. Phys.: Condens. Matter* **20**, 142201 (2008).

¹² J. Takaobushi, H. Tanaka, T. Kawai, S. Ueda, J.-J. Kim, M. Kobata, E. Ikenaga, M. Yabashi, K. Kobayashi, Y. Nishino, D. Miwa, K. Tamasaku, and T. Ishikawa, *Appl. Phys. Lett.* **89**, 242507 (2006).

¹³ J. Takaobushi, M. Ishikawa, S. Ueda, E. Ikenaga, J.-J. Kim, M. Kobata, Y. Takeda, Y. Saitoh, M. Yabashi, Y. Nishino, D. Miwa, K. Tamasaku, T. Ishikawa, I. Satoh, H. Tanaka, K. Kobayashi, and T. Kawai, *Phys. Rev. B* **76**, 205108 (2007).

¹⁴ A. Brandlmaier, S. Geprägs, M. Weiler, A. Boger, M. Opel, H. Huebl, C. Bihler, M.S. Brandt, B. Botters, D. Grundler, R. Gross, and S.T.B. Goennenwein, *Phys. Rev. B* **77**, 104445 (2008).

¹⁵ L. Neel, *Ann. Phys.* **3**, 137 (1948).

¹⁶ Y. Yafet and C. Kittel, *Phys. Rev.* **87**, 290 (1952).

¹⁷ J. Loos and P. Novak, *Phys. Rev. B* **66**, 132403 (2002)

¹⁸ R. J. McQueeney, M. Yethiraj, S. Chang, W. Montfrooij,

- T. G. Perring, J. M. Honig, and P. Metcalf, Phys. Rev. Lett. **99**, 246401 (2007).
- ¹⁹ A. Rosenzweig, Phys. Rev. **181**, 946 (1969).
- ²⁰ P. Wang, Z. Kakol, M. Wittenauer, and J. M. Honig, Phys. Rev. B **42**, 4553 (1990).
- ²¹ V. G. Harris, N. C. Koon, C. M. Williams, Q. Zhang, M. Abe, and J. P. Kirkland, Appl. Phys. Lett. **68**, 2082 (1996).
- ²² Y. Li, Q. Li, M. Wen, Y. Zhang, Y. Zhai, Z. Xie, F. Xu, and S. Wei, J. Elect. Spectrosc. **160**, 1 (2007).
- ²³ J.P. Shepherd, R. Aragon, J.W. Koenitzer, and J.M. Honig, Phys. Rev. B **32**, 1818 (1985).
- ²⁴ R. Aragón and R. H. McCallister, Phys. Chem. Minerals **8** 112 (1982).
- ²⁵ R. Aragón, D.J. Buttrey, J.P. Shepherd, and J.M. Honig, Phys. Rev. B **31**, 430 (1985).
- ²⁶ K. A. Shaw, E. Lochner, and D. M. Lind, J. Appl. Phys. **87**, 1727 (2000).
- ²⁷ A. Nielsen, A. Brandmaier, M. Althammer, W. Kaiser, M. Opel, J. Simon, W. Mader, S.T.B. Goennenwein, and R. Gross, Appl. Phys. Lett. **93**, 162510 (2008).
- ²⁸ D. T. Margulies, F. T. Parker, F. E. Spada, R. S. Goldman, J. Li, R. Sinclair, and A. E. Berkowitz, Phys. Rev. B **53**, 9175 (1996); see also D. T. Margulies, F. T. Parker, M. L. Rudee, F. E. Spada, J. N. Chapman, P. R. Aitchison, and A. E. Berkowitz, Phys. Rev. Lett. **79**, 5162 (1997).
- ²⁹ T. Hibma, F. C. Voogt, L. Niesen, P. A. A. van der Heijden, W. J. M. de Jonge, J. J. T. M. Donkers, and P. J. van der Zaag, J. Appl. Phys. **85**, 5291 (1999).
- ³⁰ R. Gross, J. Klein, B. Wiedenhorst, C. Höfener, U. Schoop, J. B. Philipp, M. Schonecke, F. Herbstritt, L. Alff, Yafeng Lu, A. Marx, S. Schymon, S. Thienhaus, and W. Mader, Proc. SPIE **4058**, 278 (2000).
- ³¹ M.E. Fleet, Acta Cryst. B **37**, 917 (1981).
- ³² J. Klein, C. Höfener, L. Alff, and R. Gross, Supercond. Sci. Technol. **12**, 1023 (1999).
- ³³ D. Reisinger, B. Blass, J. Klein, J. B. Philipp, M. Schonecke, A. Erb, L. Alff, and R. Gross, Appl. Phys. A **77**, 619 (2003).
- ³⁴ D. Reisinger, M. Schonecke, T. Brenninger, M. Opel, A. Erb, L. Alff, R. Gross, J. Appl. Phys. **94** 1857 (2003).
- ³⁵ D. Reisinger, P. Majewski, M. Opel, L. Alff, R. Gross, Appl. Phys. Lett. **85**, 4980 (2004).
- ³⁶ F. Schedin, E. W. Hill, G. van der Laan, and G. Thornton, J. Appl. Phys. **96**, 1165 (2004).
- ³⁷ A. Marcu, T. Yanagida, K. Nagashima, H. Tanaka, and T. Kawai, J. Appl. Phys. **102**, 023713 (2007).
- ³⁸ I. Barin, *Thermodynamical Data of Pure Substance*, British Library Cataloguing in Publication Data, VCH Verlagsgesellschaft, Weinheim (1989).
- ³⁹ I.G. Austin and N.F. Mott, Adv. Phys. **18**, 41 (1969).
- ⁴⁰ N.F. Mott and Z. Zinamon, Rep. Prog. Phys. **33**, 881 (1970).
- ⁴¹ D. Emin and T. Holstein, Ann. Phys. **53**, 439 (1969).
- ⁴² W. Haubenreisser, phys. stat. sol. **1**, 619 (1961).
- ⁴³ L. Alff, G. Fischer, R. Gross, F. Kober, K.D. Husemann, A. Beck, T. Nissel, C. Burckhardt, and F. Schmidl, Physica C **200**, 277 (1992).
- ⁴⁴ D. Venkateshvaran, W. Kaiser, A. Boger, M. Althammer, M.S. Ramachandra Rao, S.T.B. Goennenwein, M. Opel, R. Gross, Phys. Rev. B **78**, 092405 (2008).
- ⁴⁵ A.J. Bosman and H.J. van Daal, Adv. Phys. **19**, 1 (1970).
- ⁴⁶ M.I. Klinger and A.A. Samokhvalov, phys. stat. sol. (b) **79**, 9 (1977).
- ⁴⁷ N. Popandian and A. Narayanasamy, J. Appl. Phys. **93**, 2770 (2002).
- ⁴⁸ Z. Simsa and V.A.M. Brabers, IEEE Trans. Magn. **24**, 1910 (1988).
- ⁴⁹ G. J. Snyder, R. Hiskes, S. DiCarolis, M. R. Beasley, and T. H. Geballe, Phys. Rev. B **53**, 14434 (1996).
- ⁵⁰ Yafeng Lu, J. Klein, F. Herbstritt, J. B. Philipp, A. Marx, and R. Gross, Phys. Rev. B **73**, 184406 (2006).
- ⁵¹ Yafeng Lu, J. Klein, F. Herbstritt, J.B. Philipp, A. Marx, L. Alff, and R. Gross, phys. stat. sol. (b) **242**, 1545 (2005).
- ⁵² Yafeng Lu, J. Klein, C. Höfener, B. Wiedenhorst, J. B. Philipp, F. Herbstritt, A. Marx, L. Alff, and R. Gross, Phys. Rev. B **62**, 15806 (2000).
- ⁵³ E. J. W. Verwey, Nature (London) **144**, 327 (1939).
- ⁵⁴ N. F. Mott, Adv. Phys. **16**, 49 (1967).
- ⁵⁵ E. J. Verwey, P.W. Haayman, and F. C. Romeijn, J. Chem. Phys. **15**, 181 (1947).
- ⁵⁶ J. García, G. Subías, M. G. Proietti, J. Blasco, H. Renevier, J. L. Hodeau, and Y. Joly, Phys. Rev. B **63**, 054110 (2001); see also J. García, G. Subías, M. G. Proietti, H. Renevier, Y. Joly, J. L. Hodeau, J. Blasco, M. C. Sanchez, and J. F. Berar, Phys. Rev. Lett. **85**, 578 (2000).
- ⁵⁷ F. Walz, J. Phys.: Condens. Matter **14**, R285-R340 (2002).
- ⁵⁸ J. P. Wright, J. P. Attfield, and P. G. Radaelli, Phys. Rev. B **66**, 214422 (2002).
- ⁵⁹ I. Leonov, A. N. Yaresko, V. N. Antonov, M. A. Korotin, and V. I. Anisimov, Phys. Rev. Lett. **93**, 146404 (2004).
- ⁶⁰ S. Todo, K. Siratori, and S. Kimura, J. Phys. Soc. Japan **64**, 2118 (1995).
- ⁶¹ W. Eerenstein, T. T. M. Palstra, and T. Hibma, Phys. Rev. B **66**, 201101 (2002).
- ⁶² S. Tiwari, D. M. Phase, and R. J. Choudharya, Appl. Phys. Lett. **93**, 234108 (2008).
- ⁶³ M. L. Paramês, J. Mariano, Z. Viskadourakis, N. Popovici, M. S. Rogalski, J. Giapintzakis, and O. Conde, Appl. Surf. Sci. **252**, 4610 (2006).
- ⁶⁴ G. A. Ferguson jr and M. Hass, Phys. Rev. **112**, 1130 (1958).
- ⁶⁵ M. Viret and L. Ranno, J.M.D. Coey, Phys. Rev. B **55**, 8067 (1997).
- ⁶⁶ M. Viret, L. Ranno, and J.M.D. Coey, J. Appl. Phys. **81**, (1997).
- ⁶⁷ P. Wagner, I. Gordon, L. Trappeniers, J. Vanacken, F. Herlach, V. V. Moshchalkov, and Y. Bruynseraede, Phys. Rev. Lett. **81**, 3980 (1998).
- ⁶⁸ J. M. de Teresa, *private communication* (2008).
- ⁶⁹ A. H. Morrish, *The physical principles of magnetism*, IEEE Press, New York (2001).